Imaging Biomolecular Interactions by Fast Three-Dimensional Tracking of Laser-Confined Carrier Particles†

Volkmar Heinrich,*,‡,⊥ Wesley P. Wong,§,⊥ Ken Halvorsen,§ and Evan Evans||

Department of Biomedical Engineering and Biomedical Engineering Graduate Group, University of California at Davis, 451 East Health Sciences Drive, Davis, California 95616, The Rowland Institute at Harvard, Harvard University, 100 Edwin H. Land Boulevard, Cambridge, Massachusetts 02142, and Department of Biomedical Engineering, Boston University, 44 Cummington Street, Boston, Massachusetts 02215

Received August 31, 2007. In Final Form: November 1, 2007

The quantitative study of the near-equilibrium structural behavior of individual biomolecules requires high-resolution experimental approaches with longtime stability. We present a new technique to explore the dynamics of weak intramolecular interactions. It is based on the analysis of the 3D Brownian fluctuations of a laser-confined glass bead that is tethered to a flat surface by the biomolecule of interest. A continuous autofocusing mechanism allows us to maintain or adjust the height of the optical trap with nanometer accuracy over long periods of time. The resulting remarkably stable trapping potential adds a well-defined femto-to-piconewton force bias to the energy landscape of molecular configurations. A combination of optical interferometry and advanced pattern-tracking algorithms provides the 3D bead positions with nanometer spatial and >120 Hz temporal resolution. The analysis of accumulated 3D positions has allowed us not only to identify small single biomolecules but also to characterize their nanomechanical behavior, for example, the force−extension relations of short oligonucleotides and the unfolding/refolding transitions of small protein tethers.

Introduction

The ongoing development of ultrasensitive force probes has enabled an increasingly detailed nanomechanical examination of individual biomolecules. This in turn has revealed remarkable features of the interactions within and between single biomolecules, such as

- a low, dynamic (thermally susceptible) strength,[1,2]
- an exponentially force-dependent lifetime,[2,3] and
- great complexity, giving rise to intriguing nanoscale mechanisms that allow molecules to act as mechanical shock absorbers,[4−6] elasticlike springs,[7] or even mechanochemical switches.[8]

Two significant challenges in this field are (i) the expansion of the range of accessible time (or force) scales and (ii) the minimization of measurement uncertainties that have limited single-molecule studies to relatively strong interactions of large molecules. For example, limitations in the longtime stability of force probes have largely restricted single-molecule experiments to far-from-equilibrium approaches. Such approaches are less suited to elicit the complex, weak interactions expected to govern biomolecular function near equilibrium. The refinement of modern single-molecule techniques requires high-resolution position detection, reliable calibration of ever-more-sensitive force transducers, and precise characterization of hydrodynamic coupling effects and of the elasticity of linker molecules that are used to immobilize biomolecules on solid substrates.

We have designed a novel approach that extends earlier concepts[9−15] to meet a number of these challenges. It uses optical interferometry to provide a high-precision record of the 3D positional statistics of a glass microsphere that is tethered to a planar surface (microscope coverslip) by the molecule of interest (i.e., a single, flexible biopolymer (protein or nucleic acid; Figure 1)). An optical trap[16,17] whose position is accurately maintained over long times by a custom-designed feedback routine allows us to confine and maneuver the test bead local to the bottom of the microscope chamber. Conformational transitions of the tethered biomolecule cause stochastic interruptions in the bead motion, imprinting a distinct signature in the statistics of the 3D bead positions.

The goal of this article is to describe the design and implementation of our approach, supported by specific example measurements that demonstrate its resolution and utility. Notable

† Part of the Molecular and Surface Forces special issue.

* To whom correspondence should be addressed. E-mail: vheinrich@ucdavis.edu.

‡ University of California at Davis.

§ Harvard University.

|| Boston University.

⊥ These authors contributed equally to this work.

(1) Evans, E.; Ritchie, K. *Biophys. J.* **1997**, *72*, 1541−1555.

(2) Merkel, R.; Nassoy, P.; Leung, A.; Ritchie, K.; Evans, E. *Nature* **1999**, *397*, 50−53.

(3) Bell, G. I. *Science* **1978**, *200*, 618−627.

(4) Marszalek, P. E.; Lu, H.; Li, H.; Carrion-Vazquez, M.; Oberhauser, A. F.; Schulten, K.; Fernandez, J. M. *Nature* **1999**, *402*, 100−103.

(5) Rief, M.; Grubmuller, H. *Chem. Phys. Chem* **2002**, *3*, 255−261.

(6) Williams, P. M.; Fowler, S. B.; Best, R. B.; Toca-Herrera, J. L.; Scott, K. A.; Steward, A.; Clarke, J. *Nature* **2003**, *422*, 446−449.

(7) Schwaiger, I.; Sattler, C.; Hostetter, D. R.; Rief, M. *Nat. Mater.* **2002**, *1*, 232−235.

(8) Evans, E.; Leung, A.; Heinrich, V.; Zhu, C. *Proc. Natl. Acad. Sci. U.S.A.* **2004**, *101*, 11281−11286.

(9) Florin, E. L.; Pralle, A.; Stelzer, E. H. K.; Hoerber, J. K. H. *Appl. Phys. A: Mater. Sci. Process.* **1998**, *66*, S75−S78.

(10) Prieve, D. C. *Adv. Colloid Interface Sci.* **1999**, *82*, 93−125.

(11) Rohrbach, A.; Florin, E. L.; Stelzer, E. H. K. *Proc. SPIE* **2001**, *4431*, 75−86.

(12) Singh-Zocchi, M.; Dixit, S.; Ivanov, V.; Zocchi, G. *Proc. Natl. Acad. Sci. U.S.A.* **2003**, *100*, 7605−7610.

(13) Pouget, N.; Dennis, C.; Turlan, C.; Grigoriev, M.; Chandler, M.; Salome, L. *Nucleic Acids Res.* **2004**, *32*, e73.

(14) Blumberg, S.; Gajraj, A.; Pennington, M. W.; Meiners, J. C. *Biophys. J.* **2005**, *89*, 1272−1281.

(15) Nelson, P. C.; Zurla, C.; Brogioli, D.; Beausang, J. F.; Finzi, L.; Dunlap, D. *J. Phys. Chem. B* **2006**, *110*, 17260−17267.

(16) Sheetz, M. P. *Laser Tweezers in Cell Biology*; Academic Press: San Diego, CA, 1998; Vol. 55.

(17) Lang, M. J.; Block, S. M. *Am. J. Phys.* **2003**, *71*, 201−215.

10.1021/la7027059 CCC: $40.75
Published on Web 01/17/2008

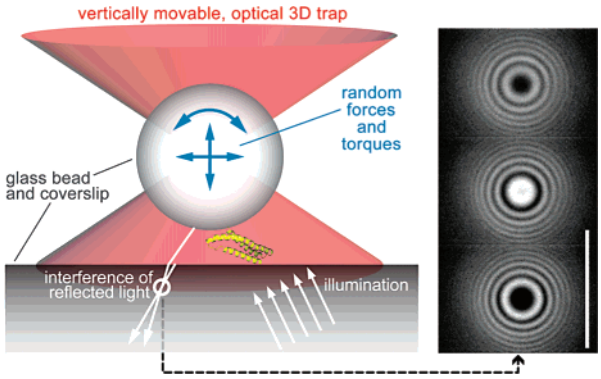

Figure 1. Sketch of a functionalized glass bead that is tethered to a reactive substrate (microscope coverslip) by a small biomolecule (shown as a triple-helical polypeptide). Random thermal forces and torques imparted by the aqueous environment cause the bead to undergo Brownian motion. A laser-optical trap confines the bead in a weak potential and allows us to apply controlled stresses to linkages between the bead and the substrate. The bead is imaged with reflection interference contrast microscopy (RICM). The light components reflected at the coverslip/buffer interface and at the underside of the bead interfere to generate a radially symmetric pattern. Example RICM patterns of the same bead (radius ~7.5 μm) at different heights are included at the right. (The white bar corresponds to 10 μm.)

achievements include the ability to continuously analyze the 3D positions of one or more moving test beads (diameters ~2−15 μm) at ~120 video images per second (where the data-acquisition speed is limited by the frame rate of our video camera). The bead positions are reported with ~1 nm lateral ($x-y$) and ~0.2 nm vertical (z) resolution, covering a height range of up to ~500 nm.

A number of advantages over existing techniques make this approach particularly well suited for measurements of near-equilibrium single-biomolecule interactions. First, rather than measuring the vertical bead positions with respect to an arbitrary (or even changing) reference frame, our use of interferometry reveals the actual distance between the test bead and the substrate, which is the primary quantity of interest. The use of reflected light allows for the easy manipulation of the test bead from above, such as lifting it from the substrate with a micropipette.[18] Owing to the high visibility of the interference pattern of a glass bead, optically thin objects or films can be placed between the test bead and the flat surface to inspect their thickness and/or transversal compressibility.[19] Further advantages include the relatively large span of vertical distances accessible to detection, the ability to carry out height measurements without having to calibrate each bead, and algorithms that can easily be scaled up to track multiple beads simultaneously.

To meet various challenges encountered during the implementation of this technique, we have developed a number of general methods that can also be of significant use in many other techniques employed by diverse research groups, such as

- fast, high-resolution algorithms for the lateral tracking of moving-image features that are radially symmetric but may otherwise change appearance,
- a continuous autofocusing feedback system that maintains the vertical position of the optical trap steady over periods of hours, ensuring long-time nanometer stability of our experiments,
- the prediction and verification of the relationship between the displacement of a laser-guiding telescope lens and the vertical travel of the laser trap, which allows for accurate adjustments of the vertical trap position without having to change the microscope's imaging focus,
- an innovative equipartition-based calibration of the spring constant of the optical trap, which accounts for the averaging effect of the camera-exposure time and allows us to correct for the otherwise substantial error caused by motion blur,[20] and
- a "Brownian-imaging" procedure that allows us to determine forces from the bead fluctuations even when an independent trap calibration is not available.

Materials and Methods

Borosilicate beads (Duke Scientific) and microscope coverslips were base washed at pH 10.9 by a 5 min boil in a ~5× diluted (in nanopure water) 1:4 mixture of 30% hydrogen peroxide and concd ammonium hydroxide. If needed, the glass surfaces were functionalized with mercaptosilane (Gelest).

In prototype experiments on single-stranded DNA, we used a synthetic 50-base oligonucleotide (IDT) that had C_{18} spacers at both ends and a 5′-acrydite and 3′-biotin modification. The acrydite group was covalently linked to mercaptosilanized coverslips (protocol by IDT, www.idtdna.com). Clean glass beads were functionalized by the physisorption of biotinylated BSA, followed by incubation with streptavidin.

Experiments involving polyprotein spectrin domains used two different engineered constructs. The first was the human αI subunit (consisting of a GST tag and five spectrin repeats, beginning with repeat 17 and continuing to the C terminus; this was a gift from Dr. Mohandas Narla, New York Blood Center). To immobilize this construct on carrier particles, the mercaptosilanized beads were further modified with an NHS-PEG3400-maleimide linker (Nektar) as described previously,[21,22] followed by attachment of an anti-α-I C antibody. The spectrin construct was then bound to the immobilized antibody by incubation in a Hepes 150 buffer (10 mM Hepes, 70 mM NaCl, pH 7.4) for 30 min. Directly before use, the beads were further passivated in 0.5% (w/v, i.e., 0.5 g per 100 mL of buffer) BSA for 30 min. Clean coverslips were functionalized by the physisorption of a mouse anti-GST antibody (2 μg/mL, Oncotech) for 30 min, followed by incubation in 1% (w/v) BSA for 45 min. The actual tethering experiments were conducted in Hepes 150 buffer with 0.05% (w/v) BSA.

The second spectrin construct consisted of four identical chicken brain R16 α-spectrin domains that were separated from one another by titin I27 domain spacers and modified at one end with a His tag (gift from Dr. Jane Clarke, MRC Centre for Protein Engineering, University of Cambridge, U.K.). A cysteine exposed at the unmodified end of this construct was biotinylated using a biotin-PEG3400-maleimide linker (Nektar). Then, the construct was attached to coverslips that had been coated with streptavidin by physisorption. As above, mercaptosilanized beads were first modified with NHS-PEG3400-maleimide. Then, an anti-penta-His antibody was covalently linked via its free amines to the beads.

Technique for Photonic Force Spectroscopy of Weak Molecular Interactions. *Instrument.* Our instrument combines a laser-optical trap with reflection interference contrast microscopy (RICM). It was built around the lower body of a Zeiss Axiovert 200 inverted research microscope equipped for epi-illumination (Figure 2). The RICM image is formed by reflected, quasi-monochromatic light (k, m) using Zeiss Antiflex optics (f, g) and a polarizing assembly (n, p, o; parts m-p, e by Chroma). Using the microscope's two video ports, the image is fed simultaneously to a SensiCam video camera (r; Cooke; http://www.pco.de) via a 4× Zeiss TV adapter at a final magnification of ~38 nm/pixel and without magnification to a second camera (t; CCD 72, DAGE-MTI). In fast-frame-rate mode, the

(18) Heinrich, V.; Rawicz, W. *Langmuir* **2005**, *21*, 1962−1971.
(19) Heinrich, V.; Ritchie, K.; Mohandas, N.; Evans, E. *Biophys. J.* **2001**, *81*, 1452−1463.
(20) Wong, W. P.; Halvorsen, K. *Opt. Express* **2006**, *14*, 12517−12531.
(21) Evans, E.; Leung, A.; Hammer, D.; Simon, S. *Proc. Natl. Acad. Sci. U.S.A.* **2001**, *98*, 3784−3789.
(22) Perret, E.; Leung, A.; Morel, A.; Feracci, H.; Nassoy, P. *Langmuir* **2002**, *18*, 846−854.

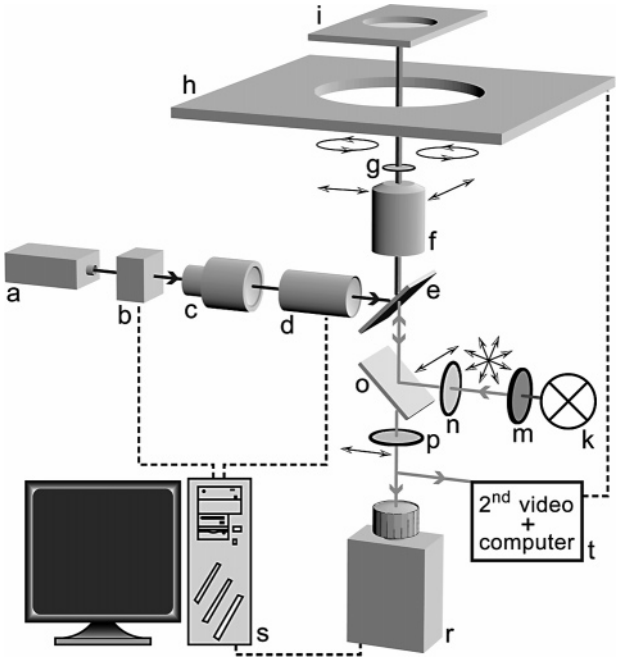

Figure 2. Schematic of the instrument for photonic force spectroscopy. The labeled parts are (a) 1064 nm CW laser head, (b) liquid-crystal power controller, (c) zoom beam expander, (d) 1× variable telescope, (e) dichroic beam splitter, (f) 63×/1.25NA Antiflex microscope objective with (g) integrated $^1/_4$-wave plate, (h) three-axis piezo-controlled microscope stage, (i) test chamber (resting on h), (k) 100 W mercury arc lamp, (m) 546 ± 5 nm interference filter, (n) polarizer, (o) polarizing beam splitter, (p) analyzer, (r) 12bit, cooled SensiCam CCD camera, (s) computer with interfaces to parts b, d, and r, and (t) second video camera and computer. The polarizing assembly (n, o, p along with g) minimizes internal reflections while maximizing the intensity of the imaging light. (Double arrows indicate the polarization direction of the propagating light.) Only light reflected at optical interfaces above the $^1/_4$-wave plate (g) contributes to the interference pattern.

SensiCam's speed depends on the number of image lines, giving ~120 images/s for the 120 video lines routinely used here. Using multithreaded Visual C++ programming and a fast computer (Windows PC with 2 GHz processor) (s), SensiCam images are analyzed in real time. The second video stream is digitized (Meteor-II, Matrox) and analyzed by another computer (t).

A laterally stationary, single-beam laser-optical trap is generated by a 500 mW Nd:YAG (1064 nm) diode laser (a; Coherent). The trapping power can be varied quickly and accurately via the analog input of the power controller (b; Brockton Electro-Optics). The beam is passed through the expander (c) and then through a 1× telescope that consists of two 5× MicroSpot objectives (d; c and the objectives for d by OFR). One objective is mounted to a piezo-driven objective positioner (PI), allowing us to change the beam divergence rapidly and thus to adjust the height of the trap center relative to the coverslip. The laser beam is inserted into the microscope's optical path directly below the objective via a dichroic beam splitter (e), which not only prevents damage to other microscope parts but also allows us to position the telescope (d) close to the microscope objective. The beam is focused to a diffraction-limited spot with the microscope objective (f). For testing and calibration purposes, vertically mounted micropipettes can be attached to a closed-loop piezo actuator (PI, not shown), allowing us to pick up single glass beads and displace them vertically by precisely known distances.

Autofocus. Our continuous autofocus mechanism performs essentially the same task that a microscopist carries out when focusing the condenser during the setup of Köhler illumination, albeit in the microscope's epi-illumination path. Part of this path, and conjugate to the image plane, is a field-stop diaphragm (a standard component of the microscope's fluorescent track) whose reflected-light image depends strongly on the objective focus. Our autofocus algorithm

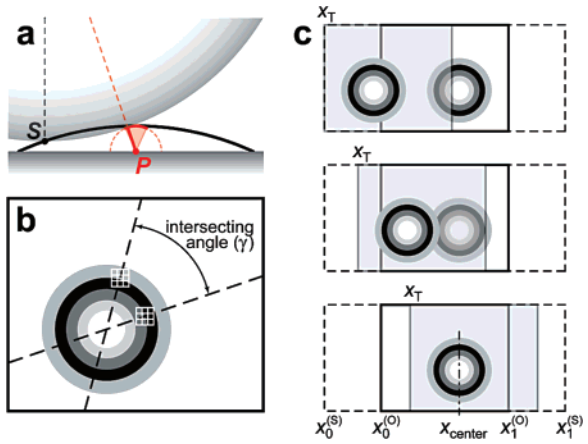

Figure 3. (a) Sketch of the geometry of a bead tethered to a flat surface at the pivot point *P*. The "south pole" *S* of the bead is the position reported by our 3D-tracking routine. (b) Weighted-center finding of intersecting intensity gradients. (c) Normalized cross-correlation with mirror images (here, in the *x* direction). The original pattern is bounded by $(x^{(O)}_0, x^{(O)}_1)$. Its mirror image is the template (grayed, transparent rectangle) that is scanned across the search region $(x^{(S)}_0, x^{(S)}_1)$ (dashed outline). The position of the left edge of the template during the scan is x_T. The maximum of the cross correlation between the template and the respective part of the underlying search region reveals the best match between the two and provides the center position x_{center} of the original pattern.

uses this dependence and monitors the drift in focus by analyzing the changing appearance of the image of the partially closed field-stop iris. Because this image is formed by reflection at the coverslip/buffer interface, it can be processed to yield a true measure of the distance between this substrate surface and the microscope objective, independent of the simultaneous tracking of beads. Our defocus measure is the variance of pixel intensities in an image region that contains part of the edge of this field diaphragm, visualized with the second computer during experiments. After a one-time calibration, automated feedback continuously corrects focus drifts to within 1 to 2 nm by vertically adjusting the piezo-driven stage (h; PI).

Vertical Trap Adjustment. The above continuous autofocus mechanism ensures that both the RICM-imaging focus and the vertical position of the optical trap remain steady over hours if desired. However, to accommodate beads of different sizes and to exert varying forces on tethered biomolecules, it is essential that the trap's vertical position can be adjusted without changing the RICM-imaging focus. In our setup, this can be done quickly by adjusting the movable lens of the telescope (part d in Figure 2). Details of our thin-lens treatment to derive the dependence of the vertical travel of the trap center Δz_{trap} on the displacement Δx_{tl} of either telescope lens are given in Appendix A. The resulting (approximate) relationship is

$$\Delta z_{trap} \cong \left(\frac{n_w}{n_g}\right)\left(\frac{f_{mo}}{f_2}\right)^2 \Delta x_{tl} \qquad (1)$$

where n_g and n_w are the refractive indices of glass and water and f_{mo} and f_2 are the effective focal lengths of the microscope objective and the telescope lens closest to the objective, respectively. (See also Figure A1.)

It is important to keep in mind that eq 1 is an approximation of the displacement of the laser focus. The actual vertical displacement of a trapped bead also depends on the (bead-size-dependent) stiffness of the optical trap (e.g., Figure 6b), which in turn may be affected by variations in the profile of the propagating laser beam. Such variations are produced in the objective's back-focal plane by telescope-lens shifts, and they are further confounded by aberrations, in particular, spherical aberration due to refraction at the coverslip/water interface.[23,24] These effects are difficult to quantify, and

(23) Wiersma, S. H.; Torok, P.; Visser, T. D.; Varga, P. *J. Opt. Soc. Am. A* **1997**, *14*, 1482−1490.

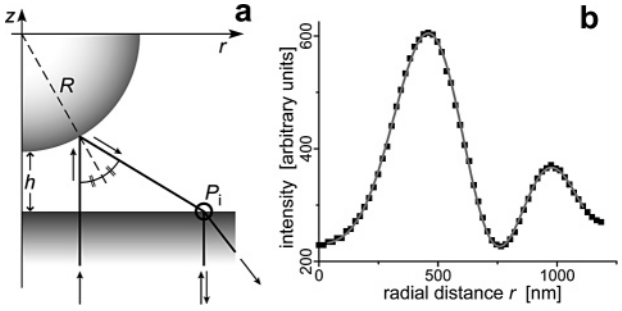

Figure 4. Determination of the bead height. (a) The simplest physical model for the formation of the observed Newton ring pattern considers the self-interference of the reflected components of an illuminating, on-axis plane wave. Strictly focusing the objective at the coverslip/buffer interface limits the analysis to the interference pattern generated in this interface (e.g., at point P_i). (b) Example fit of this model to a radial RICM intensity profile of a microsphere (~2.2 μm diameter).

although Neuman and co-workers[24] considered the simpler case of laser-focal shift via changes of the coverslip−objective distance, we agree with their conclusion that a thorough calibration is usually needed to ensure the highest confidence in one's results. As demonstrated below, we find that for the relatively small vertical displacements considered in this study eq 1 reliably predicts the vertical trap position. However, adjustments of the trapping force exerted on a tethered bead should generally be controlled via the laser power at a constant trap height, rather than changing the trap height.

Three-Dimensional Nanoscale Tracking of Microspheres near a Surface. The use of the above technique to characterize weak biomolecular interactions requires the collection of a large amount of 3D positional bead data with the highest possible precision. Whereas commercially available pattern-matching algorithms could be adapted, to some extent, to do basic tracking of moving microparticles, they are generally unsuitable for fast, high-resolution 3D position detection. First, they are often based on templates (i.e., image patterns whose appearance is assumed to remain unaltered as the tracked object changes its position and/or orientation). In contrast, the microscopic image of a small particle changes considerably whenever the particle moves perpendicular to the focal plane. Next, none of these algorithms provide positional information in the third (vertical) dimension. Finally, the majority of biologically relevant molecular interactions occur on much faster time scales than accessible by the slow, general-purpose commercial pattern-tracking routines. This section presents our approach to track the 3D positions of microspheres at high speed while achieving high precision. Because our algorithms rely exclusively on the radial symmetry of the RICM bead pattern, they can easily be adapted for the position detection of any image features exhibiting this symmetry.

The capability to record events at high speed poses another growing challenge to experimentalists: how to cope with an immense amount of acquired data. Our solution has been simple: do as much of the needed image analysis as possible in real time, and save only the results of this analysis but not the raw images. By real-time image processing, we mean the asynchronous continuous analysis of the most recently acquired image frame during the time span needed to record and transfer a new image to computer memory at whatever camera speed required or possible.

First, it is imperative for all high-speed tracking tasks to define a reduced search region within the image that is centered about a suitably chosen, searchable feature of the pattern of interest.[25] The search region should be large enough to ensure that the tracked feature will still reside inside this region when the next video image is acquired. Once the most recent position of the pattern has been identified, the search region is recentered about this new position.

(24) Neuman, K. C.; Abbondanzieri, E. A.; Block, S. M. *Opt. Lett.* **2005**, *30*, 1318−1320.

(25) Heinrich, V.; Waugh, R. E. *Ann. Biomed. Eng.* **1996**, *24*, 595−605.

As a general rule, lateral positional accuracy can be improved only at the cost of growing image-processing time. The remedy is to use a sequence of tracking algorithms that increasingly refine the position of the pattern of interest. The initial search should analyze a relatively large search region at high speed, locating the pattern center within a few image pixels. Subsequent algorithms can then utilize considerably smaller search regions, saving valuable processing time while pinpointing the center with subpixel resolution. Our sequence of up to three algorithms to find the center of the bead's interference pattern includes

- weighted center finding of intersecting intensity gradients,
- normalized cross correlation with mirror images, and
- fit to a symmetric model function with adjustable center.

Once the lateral center is found, the height h of the bead's "south pole" S relative to the bottom coverslip (Figure 3a) is obtained by fitting a simplified model to the circularly averaged, radial intensity profile. (See below.)

Lateral Center-Finding Routine for Radially Symmetric Image Patterns. Whenever the most prominent feature in an image region is radially symmetric, the majority of local intensity gradients will point either toward or away from the center of the symmetric pattern. Accordingly, our (usually) first algorithm calculates a large number of mutual intersections of straight lines defined by the directions of suitable pairs of intensity gradients (Figure 3b). To maximize speed, we bin sort the gradients by magnitude as soon as their directions and magnitudes are obtained from convolution of the search region with a Sobel gradient operator (separate 3 × 3 masks for x and y direction). A gradient pair is judged to be suitable if (i) both gradients have magnitudes greater than a chosen threshold and (ii) the angle γ between the gradients is larger than a preset value (currently 30°). The magnitude threshold is automatically adjusted to keep the total number of included intersections roughly constant (typically 300−500). The bead position is calculated as the centroid of intersections, each weighted by $\sin(\gamma)$. This robust algorithm locates the bead center reliably within ~1 pixel in usually less than 1 ms, even coping with beads that are partially obscured or have partially left the chosen search region.

As mentioned above, standard cross correlation (CC) with stored templates is unsuitable for rapidly changing, bead-height-dependent RICM patterns. Instead, we have developed a powerful CC variant, based on the notion that a radially symmetric image feature can be transformed into itself by an arbitrary reflection followed by a translation. The distance over which the mirror image needs to be translated until it matches the original pattern exposes a particular symmetry axis in the radially symmetric original. As illustrated in Figure 3c, we designate the mirror image of a rectangular image region containing the Newton-ring pattern as the template for the cross-correlation search. The search range is defined by inflating the x dimension of the original image region by a preset distance on both sides. Scanning the template pixel by pixel across the search region (cf. Figure 3c), the normalized cross correlation C is computed at each position using

$$C(x_T) = \frac{\langle ST\rangle - \langle S\rangle\langle T\rangle}{\sqrt{(\langle S^2\rangle - \langle S\rangle^2)(\langle T^2\rangle - \langle T\rangle^2)}} \qquad (2)$$

where $T(x, y)$ and $S(x, y)$ denote the intensities at a given pixel of the template and the search region, respectively. The mean intensities entering eq 2 are given by

$$\langle T\rangle = \frac{1}{N_x N_y}\sum_x\sum_y T(x - x_T, y) \qquad \langle S\rangle = \frac{1}{N_x N_y}\sum_x\sum_y S(x, y)$$

$$\langle ST\rangle = \frac{1}{N_x N_y}\sum_x\sum_y S(x, y)\, T(x - x_T, y)$$

N_x and N_y are the pixel dimensions of the template, and the summation of search-region intensities is over the respective region of overlap with the template. The maximum of the discrete function $C(x_T)$ (eq 2) gives the pixel position $\hat{x}_T$ where the template best matches the

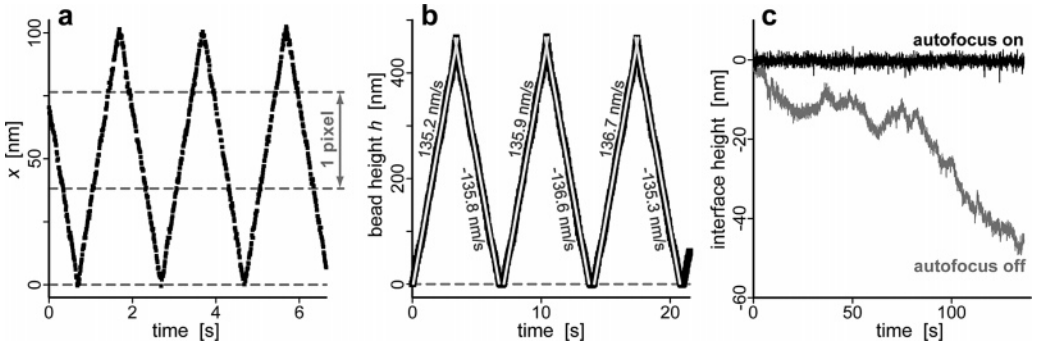

Figure 5. High-resolution tracking examples. (a) A surface-immobilized bead (2 μm diameter) was repeatedly translated in the x direction by a total of 100 nm (~2.5 image pixels) at a speed of 100 nm/s using the piezo-driven microscope stage. The bead position was determined every ~8 ms in real time. The resulting trace accurately reproduces the imposed movement with subpixel resolution. (b) Series of measured vertical positions for repeated up-and-down translation of a pipet-held microsphere (~2.5 μm diameter) at a preset speed of 137.6 nm/s using a closed-loop piezo actuator. The moment of contact between the moving bead and the coverslip defined the absolute zero height. The apparent velocity (average of the slopes of the superimposed linear fits) was 135.9 nm/s, giving a correction factor of 1.01 that needs to be applied to the measured height data in this case. (c) The autofocus mechanism successfully compensates for vertical drifts of the coverslip/buffer interface relative to the objective's focal plane. With the autofocus on, the interface height remains stable for periods of hours (shown here only for ~2 min).

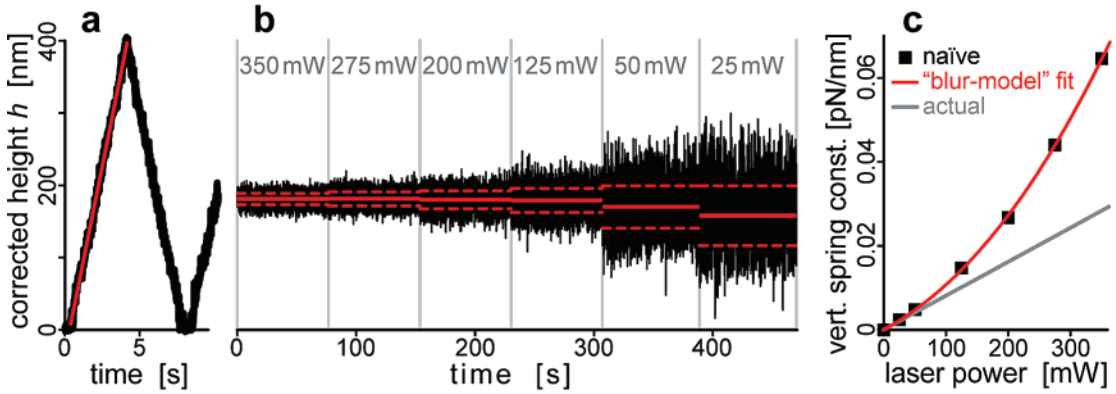

Figure 6. Examples of vertical trap manipulation based on a total of ~60 000 measurements of 3D bead positions. (a) A trapped small glass bead (~1.9 μm diameter) is moved up and down at a constant speed by adjusting the trap height with the telescope (previous section). The measured raw bead heights were corrected to give a velocity (slope of the superimposed linear fit) that was in agreement with eq 1. (b) Next, the laser power (top) was decreased in six steps at a fixed trap position. Superimposed are the average corrected bead heights (horizontal solid lines) ± standard deviations (dashed lines). (c) The vertical spring constant of the trap was found by first fitting eq 6 to the naïve spring constants (■) obtained from the variances of the data in plot b using eq 5. The fit (red line) gave a conversion factor of $c = 0.081$ pN/nm/W for the linear dependence of the actual trap spring constant on the laser power (gray line).

original image. To achieve subpixel resolution, we interpolate a small range of the CC data about $\hat{x}_T$ using a low-order polynomial and determine the maximum of this continuous fitting function. Finding two independent symmetry axes in this way, the bead center is given by their intersection.

We optionally refine the center further by choosing small and relatively short image stripes (in x and y directions) that contain the center, bin each stripe into a single line, and fit a suitable symmetric function to the resulting intensity data. An example fitting function (for the x direction) that we have used successfully is the cosine series

$$f(x - x_{\text{center}}) = \sum_{j=0}^{n} a_j \cos\left(j \frac{x - x_{\text{center}}}{w}\right) \tag{3}$$

where the values of n and w are picked at the beginning of the calculation, whereas the coefficients a_k as well as the desired x_{center} are fitting parameters. To account for (linear) intensity gradients that may be present in the image background, we usually also add the term bx to the expression given in eq 3. Another possibility is to use a Taylor expansion of the particular nonlinear fitting function that will be used below to extract the bead height from each radial intensity profile. This choice has the advantage that the function is likely to be a good approximation of the intensity profile, which means that the fit will provide good initial values for the full nonlinear height fit described next.

Vertical Position Detection of Microspheres Using Interferometry. Knowing the center of the RICM pattern of the bead, we compute the average of the radial intensity profile over all radial directions, greatly improving the signal-to-noise ratio. Then, a suitable model that predicts the profile as a function of the gap height and the bead radius is fit to the data (Figure 4). The motivation for the simple model currently used and its limitations are discussed in detail in Appendix B.

Approximating the underside of the bead as a paraboloid, the difference $\Delta\Lambda(r)$ in optical path length of the two interfering components (as described by geometrical optics) is

$$\Delta\Lambda(r) = \frac{1}{2} n_{\text{buffer}} [2h - R + \sqrt{4r^2 + (2h + R)^2}]$$

The refractive index for aqueous solutions is $n_{\text{buffer}} \approx 1.33$. All other symbols are defined in Figure 4. The resulting phase difference is

$$\Delta\Phi(r) = \left(\frac{2\pi}{\lambda_0}\right)\Delta\Lambda(r) + \pi \tag{4}$$

where $\lambda_0 = 546$ nm, and a constant phase shift of π is introduced by reflection at the higher-index bead surface. The location of interference fringes is predominantly governed by the cosine of the expression in eq 4. The much less tractable envelope of this cosine is modeled in an empirical manner. We use a constant offset (usually

fixed during fitting) and two Gaussians to describe the amplitude of the cosine and the intensity contributions of non-interfering reflected light,[26] which adds five empirical parameters ($A_{0,1,2}$ and $b_{1,2}$) to our model of the intensity I as a function of the radial distance r:

$$I(r) = A_0 + A_1 \exp(-b_1 r^2) + A_2 \exp(-b_2 r^2) \cos \Delta\Phi(r)$$

In this fitting function, the bead radius R is a relatively strong parameter. Bead-height information improves if after a test run with variable radius, R is fixed at the appropriate value in subsequent fits.

Results and Discussion

Three-Dimensional Tracking of Microspheres near a Surface. To quantify the resolution of our 3D-tracking algorithms, we first inspected the positional statistics of clean glass beads that were immobilized on the surface of clean coverslips. Approximately 1000 positions/bead were recorded. The lateral (x, y) position data were high-pass filtered (1 Hz cutoff) to remove slow lateral drift. For the recorded lateral positions, the standard deviations from the mean were typically ≤ 1 nm in both x and y for beads with diameters of ~ 2 μm. Determined by interferometry, the vertical bead positions exhibited considerably smaller standard deviations, typically ≤ 0.2 nm. These standard deviations are a measure of the resolving power of our 3D-tracking routine; they also represent the standard error in the position for each video frame. Within a more conservative 95% confidence interval, the statistical error in position detection would be 2 nm laterally (in the frequency band > 1 Hz) and 0.5 nm vertically. For beads larger than ~ 2 μm (diameter), more image pixels contribute to the circularly averaged radial intensity profile, significantly reducing the statistical error of the bead-height measurements. For example, tests with an ~ 7 μm (diameter) bead yielded a standard deviation as small as 0.3 Å for vertical bead positions.

Next, we evaluated the tracking accuracy for beads that were translated at constant velocities by subnanometer, closed-loop piezo actuation. Excellent lateral tracking resolution of a fraction of an image pixel is demonstrated in Figure 5a where the total travel distance of the bead was less than $^1/_5$ of the wavelength of the illuminating light. Our vertical detection method (Figure 5b) successfully reproduces the linearity of the bead motion over a large range of bead heights. A systematic bias in the measured velocities reflects a slight underestimation of the absolute vertical position, attributed to approximations in our RICM model. Although the deviation in velocity is an acceptable -1% in this example, we found that it generally depends on the bead size and on the illuminating numerical aperture and that it may grow progressively to as much as -10% at decreasing bead diameters. Yet for a given setup that keeps these quantities constant, a one-time calibration is sufficient to establish the appropriate correction factor that needs to be applied to all vertical tracking data. (See Appendix B for a more detailed discussion.)

The calibration of our autofocus feedback is based on measuring distance changes between the microscope objective's focal plane and the coverslip/buffer interface with nanometer accuracy. (See the previous section.) This measurement of interface height was used (Figure 5c) to demonstrate how the autofocusing routine effectively eliminates the otherwise ever-present instrument drifts that tend to displace the interface by tens of nanometers (or more) per minute.

Summarizing our 3D-tracking routine, we find that nanometer resolution is reliably achieved with glass beads with diameters larger than ~ 1.5 μm. The position detection improves both laterally and vertically with increasing bead size. However, because the trapping stiffness of optical tweezers decreases for objects that are large compared to the wavelength of the trapping laser, we prefer to use beads in the range of $2-5$ μm (diameter). It is also important to keep in mind that our RICM-based detection of the vertical bead position assumes that the surfaces of the coverslip and of the test bead are locally smooth and that surface roughness may occasionally introduce a small bias into the measured values of absolute bead height and tether length.[14,27]

Three-Dimensional Characterization and Manipulation of the Optical Trap. Careful calibration of the optical trap's spring constant is an essential prerequisite for the application and measurement of minuscule forces. A common calibration method is based on the confined fluctuations of a trapped particle (tracked, for example, in the x direction). The spring constant is identified with the ratio of the thermal energy $k_B T$ and the variance of the measured particle positions

$$k_{\text{naïve}} = \frac{k_B T}{\text{var}(x)} \tag{5}$$

as prescribed by the equipartition theorem. This method, however, is not without peril. In fact, if the particle positions are compiled from images taken with a standard video camera, then the resulting $k_{\text{naïve}}$ will substantially deviate from the actual spring constant k. This is demonstrated in Figure 6c, revealing a nonlinear laser-power dependence of the vertical naïve spring constant (obtained using our bead-height detection method and eq 5), contrary to the expected linear dependence of the actual trap stiffness k. This behavior has recently been analyzed in detail.[20] It was confirmed that the averaging effect of finite camera-exposure times or any other averaging that occurs during the finite acquisition times of individual data points can significantly reduce the variance of the measured positions, which in turn results in an overestimate of the naïve stiffness of the confining potential. Fortunately, this "motion-blur" effect can be corrected for relatively easily, and it can even be used to expose interesting information about the bead dynamics on time scales faster than the video frame rate.[20] The predicted laser-power dependence of $k_{\text{naïve}}$ is

$$k_{\text{naïve}} = \frac{cP}{2}\left[\frac{1}{\alpha} - \frac{1 - \exp(-\alpha)}{\alpha^2}\right]^{-1} \tag{6}$$

where P is the laser power, c is the calibration factor that converts laser power into the actual spring constant, and $\alpha = cPt_e/\gamma$ is a dimensionless quantity that incorporates, in addition to c and P, the camera exposure time t_e and the friction factor γ.[20] A fit of this blur model to the measured values of $k_{\text{naïve}}$ involves only two fitting parameters: c and the ratio t_e/γ. Excellent agreement between this model and our $k_{\text{naïve}}$ data is demonstrated in Figure 6c. The actual trapping spring constant k is then simply the product cP.

Figure 6a,b uses the same bead to demonstrate the two modes of vertical trap adjustment: the controlled displacement of the vertical trap position by piezo translation of the moveable lens of a laser-guiding telescope and the tuning of the vertical spring constant of the trapping potential via a laser power controller (cf. Instrument subsection and previous paragraph). The travel Δx_{tl} of either telescope lens and the vertical displacement Δz_{trap} of the trap center are related by eq 1. This approximation predicts $\Delta z_{trap} \approx 0.00373 \Delta x_{tl}$ for our setup, which gives a range of ~ 1.3 μm in vertical trap displacement for the total travel (350 μm) of the piezo-mounted telescope lens. We verified eq 1 by repeatedly

(26) Radler, J.; Sackmann, E. *Langmuir* **1992**, *8*, 848−853.

(27) Zocchi, G. *Biophys. J.* **2001**, *81*, 2946−2953.

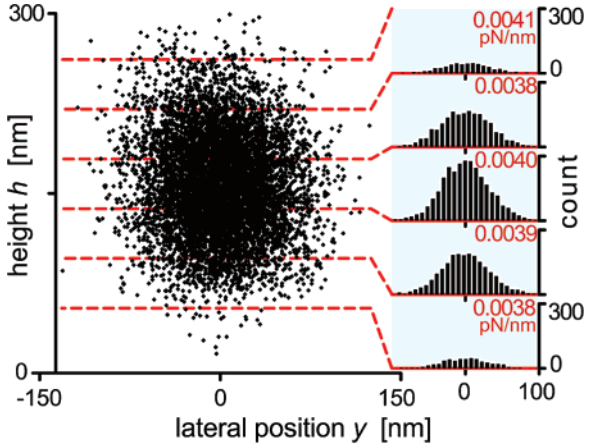

Figure 7. Scatter plot (left) of the 25 mW data of Figure 6b, projected along the *x* axis onto the *y*−*z* plane (side view). Dashed lines divide the data into five horizontal slices (each 41.5 nm high). The *y* positions within each slice were collected into the individual histograms on the right (after high-pass filtering to remove lateral drift). Each histogram includes the naïve lateral (*y*) spring constant of the trapping potential for the respective height slice, obtained by dividing k_BT by the variance of its subset of *y* positions.

moving the same bead up and down using first a piezo-mounted vertical pipet (cf. Figure 5b) and then the telescope (e.g., Figure 6a). The good agreement (to within 5% or better in velocity) for beads of less than ∼3 μm (diameter) makes it possible to replace the pipet-based height calibration with the much simpler procedure using the telescope. (The agreement was less satisfactory for larger beads whose translation is more affected by small changes in the 3D trapping potential at varying heights. As discussed above, however, the height detection of larger beads does not require calibration.) All data in Figure 6 are shown after the correction required to match the measured bead velocity to the prediction of eq 1. The amount of sagging of the average bead position at decreasing trapping powers (Figure 6b) is set by the bead's weight. A linear fit to the mean bead height as function of the inverse (actual) vertical spring constant gives a slope that is exactly the negative bead weight discounted by buoyancy. For this example, we obtained a weight of 0.051 pN, corresponding to a bead radius of ∼939 nm, which is very close to the value of ∼935 nm estimated from the RICM pattern (using a nominal density of 2.5 g/cm^3 for the glass bead and a water density of 1 g/cm^3).

Figure 7 demonstrates another useful measurement made possible by our 3D-bead-detection routine. The scatter plot of *y*−*z* positions exposes a side view of the confining 3D potential of the optical trap. By calculating the variances for lateral (*y*) displacements for distinct height slices, we were able to validate experimentally an assumption that is implicitly made in many force measurements using optical tweezers: that the lateral spring constant is not affected by the fluctuating vertical distance of a trapped particle from the focus of the laser beam.

Application to Biomolecules. The 3D-positional statistics of a bead that is attached via a biomolecular tether to the substrate encodes specific information about this tether. In the absence of an external field, the random 3D positions of the lowest point *S* (south pole) of a singly tethered bead are bounded by a spherical cap with radius $R + L$ whose center lies at a distance of *R* below the tether's pivot point *P* (cf. Figure 3a; *R* is the bead radius and *L* is the maximum tether length). The distribution of positions inside this cap depends on the tether flexibility—including the angular freedom at its two attachment points—and on the weight of the bead. Figure 8a,b demonstrates the clear distinction of two biomolecular tethers with different flexibilities. Similarly, the 3D Brownian motion of a bead that is linked via two tethers to the substrate is more or less constrained to an arc,[28] allowing us to distinguish easily between single and multiple attachments. (The diameter of all beads used in this subsection is ∼2 μm.)

Manipulation of the optical trap allows us to inspect biomolecular responses to force steps and ramps. Whenever the trap is not perfectly aligned above a tether's pivot point on the substrate (Figure 8c), vertical distance information alone is not sufficient to characterize the biomolecule. The capability to track bead positions in 3D allows us to recover the needed information easily, yet because of random bead rotations, the shortest distance between *P* and the bead surface does not necessarily coincide with the end-to-end length of the tether, particularly at zero or low trapping forces. However, whenever the net-pulling force exceeds the polymer force scale k_BT/(segment length), it is safe to assume that bead rotations are sufficiently suppressed and that the distributions of pivot-to-bead distances (e.g., inset in Figure 8c) reflect fluctuations of the true tether length.

Next, the gradual stretching of a ssDNA tether by repeated force ramps (Figure 9a) revealed a progressive reduction in the magnitude of fluctuations of the tether's end-to-end length at larger extensions. This gives rise to the following Brownian-imaging approach to establish force−extension relations even if an independent force calibration is unavailable. If the potential governing the residual motion of the confined (tethered and trapped) bead is locally harmonic about equilibrium, then its effective spring constant at any given tether length is $k_{eff}(d) = k_BT/\mathrm{var}(d)$. Here, var(*d*) is the sliding variance of the instantaneous pivot-to-bead distance, *d*, calculated relative to a sliding average that had been computed in a previous first pass over the data. Generally, k_{eff} is the sum of the stiffness of the optical trap and of the local spring constant $k_p(d)$ of the polymer tether (including soft linker molecules). Assuming that k_p is the dominating contribution to the sum, k_{eff} may be taken as a rough estimate of k_p. Then, the force required to extend the tether from some initial length d_0 to *d* is $f_0 + \int_{d_0}^{d} k_p(\tilde{d})\, d\tilde{d}$, where f_0 is the holding force at a length of d_0. Carrying out the integration by direct evaluation of the area under the noisy $k_p(d)$ curve gives the mean force $\bar{f}(d)$ as a function of the tether length (Figure 9b). This preliminary example demonstrates the technique's potential for extracting structural properties of small single molecules by analyzing near-equilibrium thermal-noise fluctuations in the presence of a stable, slowly varying (effectively adiabatic) external potential.

Our final example highlights the ability of our technique to resolve length changes that accompany reversible intramolecular transitions of small proteins (Figure 10). In this case, the optical trap was used to subject a spectrin construct of four identical repeats to a pull/hold/return force protocol. During the loading phase, the trap laser power was increased at a preset constant rate that resulted in a force ramp with a slope of ∼5 pN/s. (Strictly, this force-loading rate is experienced by trapped objects constrained at a fixed height). Four sudden steps in length can be distinguished clearly during this loading phase (labeled by arrows in Figure 10b), corresponding to four successive unfolding events of individual spectrin repeats. Then, following a pause of 3.5 s, the trapping power was decreased at the same rate. The initial part of the return phase reveals a force−extension behavior of the unfolded construct that is well described by the wormlike chain (WLC) model (Figure 10a). However, as the decreasing

(28) Wong, W. P.; Heinrich, V.; Evans, E. *Mat. Res. Soc. Symp. Proc.* **2004**, *790*, P5.1.1−P5.1.12.
(29) Smith, S. B.; Cui, Y.; Bustamante, C. *Science* **1996**, *271*, 795−799.

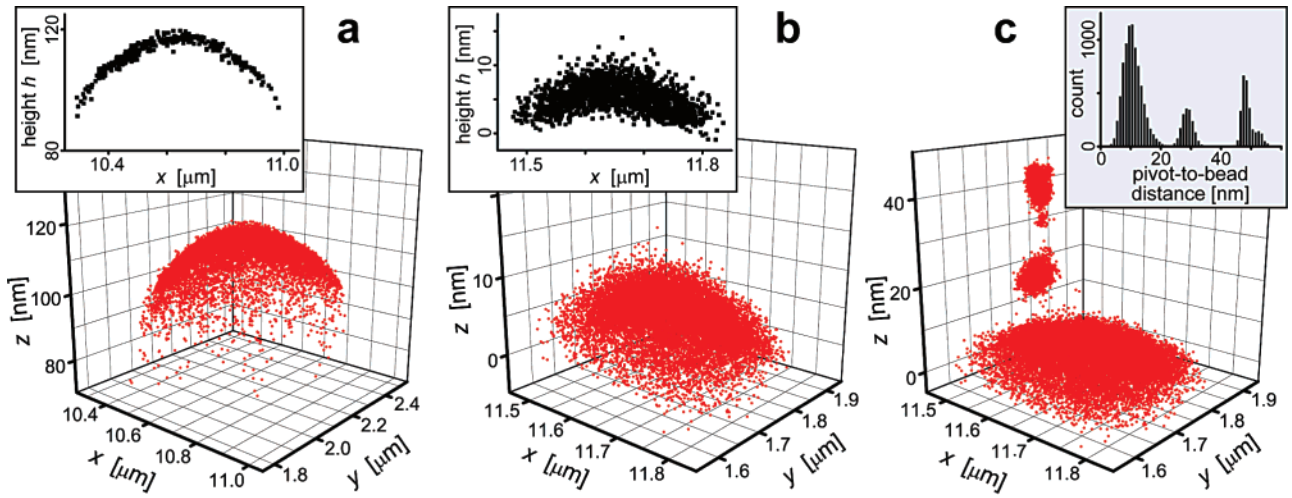

Figure 8. Characterization of short, tethered biomolecules. (a) A hollow spherical cap of 3D bead positions is the signature of a rigid biomolecular tether (here, a construct of five spectrin repeats). (b) For a flexible tether (here, a short ssDNA oligonucleotide), the cap appears to be filled. The insets in plots a and b show $x-z$ projections of a central thin slice ($\Delta y = 20$ nm) through the 3D data. Note that there is an ~10-fold difference in the z scale between plots a and b. (c) Added to the data of plot b are the positions of the bead's south pole for two nonzero trapping potentials stretching the ssDNA molecule. The optical trap was not perfectly aligned laterally with the pivot point P. The inset presents a histogram of the shortest distance between P and the bead surface.

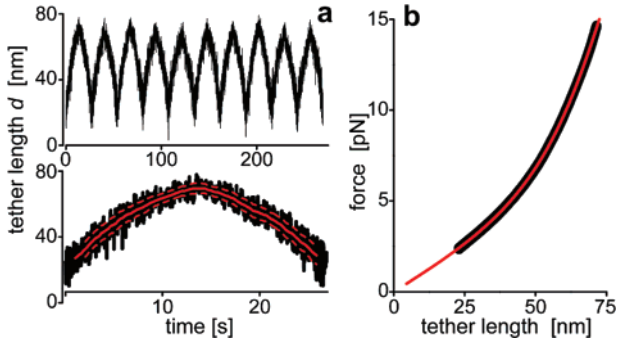

Figure 9. Mechanical characterization of a short, tethered oligonucleotide. (a) Linear up/down ramps in laser power produced continuous changes in the pivot-to-bead distance (≈ tether length d) for a ssDNA-tethered bead. The first cycle is enlarged (bottom). Superimposed is the sliding average of d (−) ± the sliding standard deviation (---). (b) Force−extension curve for the short ssDNA tether of plot a. The mean force was extracted directly from the near-equilibrium fluctuations of the tether length. High-density data symbols are shown as a thick line. The superimposed fit was obtained by modeling the inverse data as $d(f) = L(\coth t - 1/t) + (f - f_0)/k_S$, where $t \equiv b(f - f_0)/(k_BT)$ for a freely jointed chain, and an elastic term (spring constant k_S) accounts for substrate compliance. L and b are the polymer's contour length and Kuhn segment length, respectively. The fit gave $b \approx 1.7$ nm for this prototype example, in good agreement with literature values for ssDNA.[29]

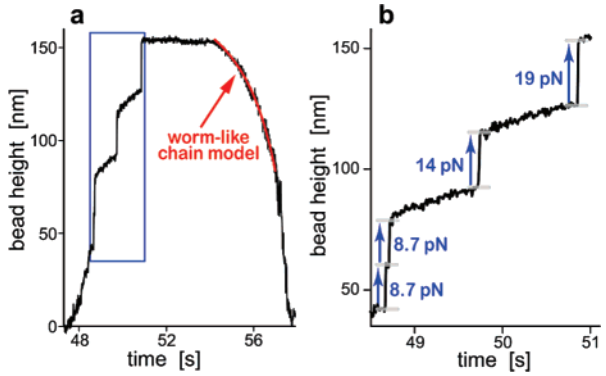

Figure 10. Unfolding of short spectrin repeats by mechanical force. The force was linearly ramped from 0.3 to 19 pN at a rate of 5 pN/s, held for 3.5 s, and then linearly decreased back to 0.3 pN at the same rate. The inset of plot a is enlarged in plot b to illustrate the exquisite resolution with which our technique reported successive unfolding events of all four spectrin repeats of the construct that was used. (Unfolding events are labeled by vertical arrows and by the respective unfolding forces.) The force−extension behavior of the unfolded construct is exposed during the initial stage of the force relaxation in plot a; it is well described by the worm-like chain model with a total contour length of 225 nm and a persistence length of 0.66 nm. Close inspection of the tether length at lower forces during the return phase reveals spectrin refolding events.

force drops below ~5 pN, the recorded protein-tether length deviates from the behavior predicted for the extended construct by the WLC model. Close inspection reveals that the spectrin repeats are refolding to their original dimension at this stage. To quantify the refolding events, we have designed and applied other force protocols more suited for this purpose; a detailed analysis is beyond the scope of this article and will be published separately.

Conclusions

This article presents the details of our new instrument and approach to quantify weak intramolecular interactions of even small biomolecules. We have demonstrated the technique's capability of high-resolution tracking of the 3D motion of functionalized carrier beads. Precise control of a well-characterized, vertically adjustable laser-optical trap allows us to superimpose longtime-stable bias potentials on the energy landscape of the biomolecular interaction of interest. Together, the advanced features of our technique pave the way toward the study of complex, ultraweak near-equilibrium interactions that have largely evaded existing approaches. A particular strength of our setup is that it is not limited to large molecules but can also interrogate biomolecular tethers as short as a few tens of nanometers. Using this technique, we have recently been able to explore the unfolding and refolding kinetics of individual spectrin repeats as a function of force (to be published).

By accumulating a bead's 3D positional statistics, we effectively utilize the minuscule Brownian impulses imparted by the environment to directly image the free-energy potential of interactions within a biomolecular tether that is immobilized between the bead and the substrate. Moreover, by manipulating the optical trap we can easily adjust the size and position of its

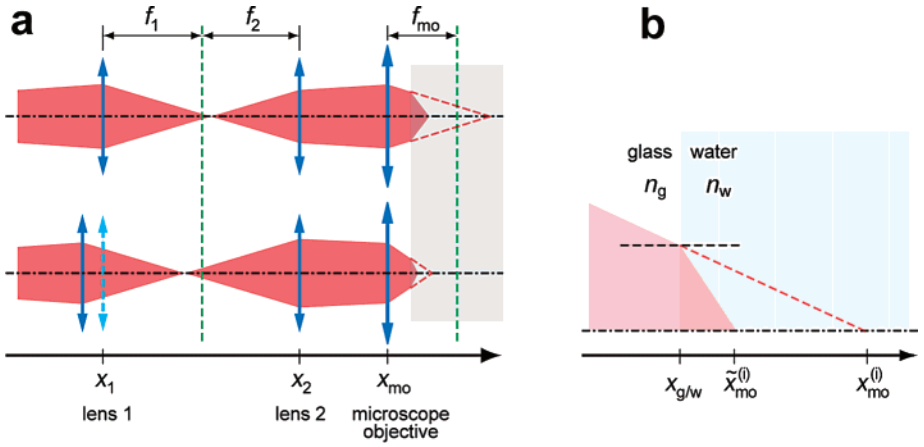

Figure A1. Displacement of the beam focus by on-axis translation of one of the two telescope lenses (here, lens 1). (a) A beam (here, originally slightly diverging) passes through telescope lenses 1 and 2 and through the microscope objective. The focal lengths of all lenses are shown at the top. Moving lens 1 toward the incoming beam by Δx_1 (bottom) displaces the apparent beam focus (i.e., the focus in the shaded immersion medium located at the intersection of the dashed red lines with the optical axis) by $\Delta\tilde{x}^{(i)}_{mo}$. (For notation, see enlarged detail in plot b.) (b) Because of refraction at the glass/water interface at $x_{g/w}$, the true beam focus moves only by $\Delta\tilde{x}^{(i)}_{mo}$. ($n_g$ and n_w are the refractive indices of the two media.)

confining potential (cf. Figures 6 and 7) and thus shape the combined energy landscape in such a way that otherwise hidden features and sparsely populated states become accessible to this Brownian-imaging approach. Essential for measurements collecting a large amount of data, the recent successful implementation of a continuous autofocusing mechanism ensures that both the trap center and the imaging focus are maintained to within 1 to 2 nm of the desired position over periods of hours.

The ability to track the 3D motion of a bead at high speed gives rise to a number of new approaches to the study of not only biomolecular statics but also nanoscale dynamics of various kinds of soft matter. Such future applications require separating the dynamics of the bead motion from the usually faster molecular interaction kinetics and relaxation times of polymer tethers. To maximize the information gained from our experiments, we have developed a multiscale Brownian dynamics simulation as an integral part of the data analysis.[28] This simulation fully accounts for the 6D random bead motion, including the hydrodynamic coupling of translational and rotational motion near a wall. The molecular-scale kinetics are coarse-grained as interacting spatial probability densities, with transition rates that are exponentiated by force as prescribed by dynamic force spectroscopy.[1,3]

The wide range of biomolecular applications of the present technique includes the measurement of kinetic rates of bidirectional transitions, such as the formation/release of bonds or the folding/unfolding of proteins, as well as the study of complex molecular interactions that may involve multiple unbinding pathways or metastable states. For example, the exquisite resolution of our instrument allows us to characterize the properties of custom-synthesized short oligonucleotides with exactly known base-pair content and sequence. This facilitates the systematic quantification of base-pair-specific contributions to the structure and energetics of both single- and double-stranded nucleic acids and their interactions with proteins. Finally, we anticipate using this technique to quantify not only intramolecular but also intermolecular interactions. In the latter case, the surfaces of the carrier bead and the flat substrate will be functionalized with the biomolecular "reactants" of interest (e.g., specific receptor/ligand pairs), and the optical trap will be used to translate the bead to/from contact with the substrate.

Acknowledgment. This work was supported by National Institutes of Health grants HL65333 and HL31579. We greatly appreciate the contribution of recombinant spectrin constructs prepared in the laboratories of Dr. Mohandas Narla (New York Blood Center) and Dr. Jane Clarke (MRC Centre for Protein Engineering, University of Cambridge, U.K.).

Appendix A

Dependence of the Vertical Displacement of the Optical Trap on the Translation of Either Telescope Lens. The height of the optical trap can be changed quickly by adjusting a movable lens of the laser-guiding telescope (part d in Figure 2) as illustrated in Figure A1. Here, we present the details of our thin-lens treatment to predict the approximate relationship between the travel Δx_1 of lens 1 of the telescope and the displacement of the vertical trap position $\Delta\tilde{x}^{(i)}_{mo}$. (If lens 2 is moved instead of lens 1, then the resulting relationship will be the same except that Δx_2 replaces Δx_1.) We start from the thin-lens law in Cartesian form

$$\frac{1}{f} = \frac{1}{x_1 - x_1^{(o)}} + \frac{1}{x_1^{(i)} - x_1} \tag{A1}$$

where x_1, $x_1^{(o)}$, and $x_1^{(i)}$ denote the positions of the lens, object, and image, respectively. Applied to the three lenses in Figure A1 (bottom; for notation see the Figure),

$$\frac{1}{f_1} = \frac{1}{x_1 + \Delta x_1 - x_1^{(o)}} + \frac{1}{x_1^{(i)} - x_1 - \Delta x_1} \tag{A2}$$

$$\frac{1}{f_2} = \frac{1}{x_1 + f_1 + f_2 - x_1^{(i)}} + \frac{1}{x_{mo}^{(o)} - x_1 - f_1 - f_2} \tag{A3}$$

$$\frac{1}{f_{mo}} = \frac{1}{x_{mo} - x_{mo}^{(o)}} + \frac{1}{f_{mo} + \Delta x_{mo}^{(i)}} \tag{A4}$$

Equation A.3 has taken into account that the initial positions of lenses 1 and 2 are related by $x_2 = x_1 + f_1 + f_2$. It further makes use of the fact that the image position of lens 1 is the object position of lens 2, $x_1^{(i)} = x_2^{(o)}$, just as $x_2^{(i)} = x_{mo}^{(o)}$. As a suitable reference position for the objective's image position, we choose $x_{mo} + f_{mo}$ so that $\Delta x_{mo}^{(i)} \equiv x_{mo}^{(i)} - (x_{mo} + f_{mo})$, which ensures that $\Delta x_{mo}^{(i)}$ is small.

The position of the laser source $x_1^{(o)}$ sets the divergence of the incoming beam (which we allow to be nonzero for generality).

However, because the beam will still be nearly parallel, the magnitude of $x_1 - x_1^{(o)}$ is very large so that $1/(x_1 - x_1^{(o)})$ is of first order in Δ or smaller. Then, a first-order expansion of eq A.2 gives

$$x_1^{(i)} - x_1 - \Delta x_1 \cong \frac{1}{\frac{1}{f_1} - \frac{1}{x_1 - x_1^{(o)}}} \cong f_1 + \frac{{f_1}^2}{x_1 - x_1^{(o)}}$$

$$x_1^{(i)} - x_1 \cong f_1 + \Delta x_1 + \frac{{f_1}^2}{x_1 - x_1^{(o)}} \tag{A5}$$

where the last two terms are small quantities. The third lens law (eq A.4) is approximated by

$$x_{mo}^{(o)} \cong x_{mo} - \frac{{f_{mo}}^2}{\Delta x_{mo}^{(i)}} \tag{A6}$$

Inserting both eqs A.5 and A.6 into the second lens law (eq A.3) gives

$$\Delta x_{mo}^{(i)} \cong \left(\frac{f_{mo}}{f_2}\right)^2 \Delta x_1 + \frac{\left(\frac{f_1 f_{mo}}{f_2}\right)^2}{x_1 - x_1^{(o)}}$$

Because the last term is a constant offset that is negligibly small for nearly parallel incoming beams, we rewrite

$$\Delta x_{mo}^{(i)} \cong \left(\frac{f_{mo}}{f_2}\right)^2 \Delta x_1 \tag{A7}$$

The difference between $x_{mo}^{(i)}$ and the actual beam focus $\tilde{x}_{mo}^{(i)}$ (due to refraction at the glass/water interface, cf. Figure A1b) is easily incorporated via Snell's law, leading to $\Delta\tilde{x}_{mo}^{(i)} \cong (n_w/n_g)\Delta x_{mo}^{(i)}$ in a small-angle approximation. Finally, the sought relationship for the vertical travel of the optical trap is found to be

$$\Delta\tilde{x}_{mo}^{(i)} \cong \frac{n_w}{n_g}\left(\frac{f_{mo}}{f_2}\right)^2 \Delta x_1 \tag{A8}$$

Identifying $\Delta z_{trap} \equiv \Delta\tilde{x}_{mo}^{(i)}$ and accounting for the interchangeability of Δx_1 and Δx_2 by using Δx_{tl} instead, we arrive at eq 1 of the main text.

Appendix B

Notes on the RICM Model for the Determination of Vertical Bead Positions. Ideally, the model function used to predict RICM patterns would be completely based on the underlying physics, for example, allowing for variations in illumination (lamp focus and angular spectrum) and changes in the position of the microscope's focal plane (which in turn also affects the illumination). This complete model would have to include the effects of partial coherence, polarization, and the focus-dependent 3D point-spread function of the microscope, not to mention aberrations introduced by the optical system. Despite a fair number of publications devoted to RICM theory, such a comprehensive description does not seem to exist at this point. It appears unlikely that an analytical solution to the complete problem can be found, and real-time correlation of a comprehensive numerical model with experimental data is impractical. Clearly, a number of simplifications are required, starting with an experimental setup that keeps as many parameters as possible fixed and well defined. This is the main reason that we restrict our present analysis to spherical particles. In addition, we devote considerable care to lamp alignment and choice of objective focus. Even so, it is crucial to verify the validity of the chosen model independently, as is done in the Results section of the main text.

Unlike most light-collecting interferometers, the Antiflex setup is an imaging system that relays an existing interference pattern from the microscope's object space to the video camera. To predict the recorded pattern, we thus need to consider mutually coherent light components that are back-scattered from the two reflecting surfaces and intersect in the thin, ideally 2D object slice in the focal plane of the high-NA microscope objective. For the used (Köhler) epi-illumination with an extended, quasi-monochromatic light source that consists of spatially incoherent point sources, interference is generated predominantly by the reflected components originating from the same illuminating plane wave. (Note that for the given bandwidth the self-coherence length of the illumination is significantly longer than any path difference considered.)

As reported earlier,[19] the RICM pattern is very sensitive to focus changes. Therefore, we always focus the objective at the same, conveniently chosen plane in all experiments (i.e., the coverslip/buffer interface). This focus is maintained with high precision and over long times using the autofocus mechanism described in the main text. (Any necessary vertical adjustments of the optical trap are made exclusively with the telescope; see the main text.) The remaining task is to compute the interference pattern that is generated by a given illuminating plane wave in the coverslip/buffer interface and to integrate the result over all possible illuminating angles. For small illuminating numerical apertures, we found that numerical results obtained with this approach were well approximated by a model that considers only the single illuminating plane wave traveling along the direction of the microscope's optical axis (cf. Figure 4). Because we can indeed limit the range of illuminating angles by reducing the diameter of the illuminating beam with the iris diaphragm conjugate to the objective's back-focal plane, this very simple model has currently become our model of choice.

Generally, this model has been found to reproduce the linearity of well-controlled vertical bead motions successfully (Figure 5b). A systematic bias in the velocity of tracked beads is discussed in the main text. In addition to this easily corrigible bias, we also occasionally observed small periodic deviations from ideal linear traces that became more noticeable at decreasing bead sizes, introducing a local error of up to ~5% in the raw bead-height data. The correction of these small deviations requires a calibration curve based on data such as that shown in Figure 5b, which can then be used to restore single-nanometer accuracy over the entire range of heights. We are currently evaluating improved RICM models for their potential to eliminate the need for this calibration even for smaller beads.

LA7027059